# Structural Architectures for Self-Erecting Lunar Towers

Jacob G. Daye * and Andrew J. Lee†
*North Carolina State University, Raleigh, NC 27695, USA*

Juan M. Fernandez ‡
*NASA Langley Research Center, Hampton, VA 23681, USA*

**The load carrying performance for deployable lunar tower architectures utilizing thin-ply composite booms are parametrically evaluated in this paper. These self-erecting towers support a communications and sensor platform on the lunar surface. The primary design consists of the corrugated rollable tubular boom (COROTUB) acting as the primary mast of the tower which supports the payload tip mass. Guy wires connecting the boom tip to spreader bars attached at the base deployer serve to correct any lateral eccentricities and provide dimensional stability. The analysis compares the maximum tip mass that this primary design can carry relative to a reference design that does not contain any guy wires or spreader bars. The results provide insights into whether the additional system mass and complexity associated with the cable-stayed design is worth the increased payload mass that can be supported. By setting the design limiting condition to a nominal maximum allowable deflection, the analysis reveals that primary design outperforms reference design for the majority of the design space. This outcome is found to be the case when the spreader bar length relative to the tower height exceeds a critical value. The analysis is extended to lunar towers with collapsible tubular mast (CTM) booms, and similar trends are observed.**

## I. Introduction

As the NASA Artemis program strides further towards manned expeditions to both the moon and Mars, the need for lightweight yet stiff extraterrestrial structures and architectures becomes ever more pressing. For any extraterrestrial-bound structure to be viable for transport to and operation on planetary surfaces, it must retain sufficient dimensional stability while minimizing packaged volume and total system mass. The NASA Langley Research Center (LaRC) led Self-Erectable Lunar Tower for Instruments (SELTI) project is a compact, lightweight, and multifunctional tower that could deploy and support multiple payloads including antennas, power and data relays, local wireless networks, optical stereo cameras, and a scanning lidar [1]. The weak lunar gravity and lack of atmosphere enables deployable composite booms to be the load-bearing mast that supports the payload.

The corrugated rollable tubular boom (COROTUB) is the primary thin-ply composite boom design being considered for SELTI [2]. The SELTI deployment mechanism and COROTUB boom are shown in Fig. 1 along with the deployment mechanism that stores the coiled boom in an enclosed volume and provides a stable deployment path from the tower base. To demonstrate the rigor of the analysis, and to provide alternative booms for comparison, a second design based on the collapsible tubular mast (CTM) is also considered [3–5]. CTM booms have been the focus of recent studies on developing torsionally stiff coilable composite structures for solar sails [6–8] and they can offer smaller cross-sections for reduced-scale versions of SELTI.

Manufacturing defects and long-term stowage-induced creep from viscoelastic stress relaxation of the composite boom material will impart initial axial curvature, or lateral deflection, on the booms upon deployment [9, 10]. These imperfections are exacerbated by thermal deformations and base tilt, which are both dependent on the location and condition of the lunar surface. When these effects are combined, the tower will exhibit lateral eccentricity that causes the payload platform to deviate from its intended position in addition to compromising dimensional stability. The primary baseline design for SELTI consists of spreader bars attached to the base deployer, which both tension and support guy wires connected to the tip of the tower. The wire tension is used to correct the aforementioned lateral eccentricity, and its effectiveness is determined by both the tension itself and the ratio of the spreader bar length to the tower height. Cable-stayed architectures of past studies provide evidence of efficacy for applications such as large deployable space

*Graduate Student, Department of Mechanical and Aerospace Engineering, 1840 Entrepeneur Dr., Campus Box 7910. AIAA Student Member.
†Assistant Professor, Department of Mechanical and Aerospace Engineering, 1840 Entrepeneur Dr., Campus Box 7910. AIAA Member.
‡Research Aerospace Engineer, Structural Dynamics Branch, NASA LaRC, 4 West Taylor St., MS 230. Senior AIAA Member.

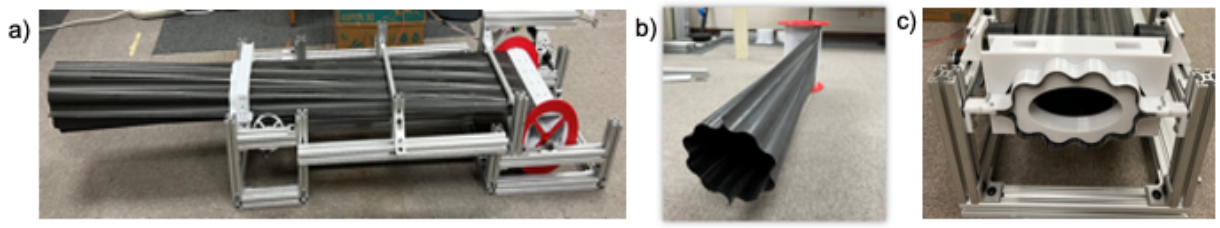


**Fig. 1 (a) SELTI protoype deployment mechanism, (b) COROTUB boom partially deployed from a spool without deployment housing showing the boom transition length from flat to deployed, and (c) deployer and plug cross-section.**

structures for solar reflectors [11], antennas [12, 13], and tension-aligned large aperture sensorcraft [14]. A need exists for optimizing both the cable tension and the tower geometry to maximize the deflection correction offered by the cable-stayed design. The tower height dictates the line-of-sight and range of coverage for autonomous robots and rovers operating on the lunar surface. Therefore, another key design objective is to maximize this height as well as the payload mass that can be supported while retaining structural stability and shape accuracy.

An analytical framework is developed and parametric design studies are conducted for lunar tower architectures to both optimize and evaluate their load-carrying capacities. The primary cable-stayed design is compared against an alternative reference design that does not utilize spreader bars or guy wires. This type of comparative study have been performed in the past to determine the efficacy of lightweight architectures on deployable spacecraft structures [15–18]. To keep the comparison consistent between the two designs, their boom length (equal to the tower height), cross-sectional profile, material properties, initial eccentricity, deflection limits, and directions are kept identical. The purpose of this analysis is to quantify the margin of advantage that eccentricity correction provides when considering the maximum payload mass that can be realistically supported.

## II. Analytical Framework

The primary cable-stayed lunar tower is referred to as design A while the unsupported reference tower is referred to as design B. Both designs include identical COROTUB booms housed in deployment mechanisms that will control the extension of the boom from the packaged, coiled state to the fully extended operational state. The functional difference between the two designs is the inclusion of three spreader bars in design A. These spreader bars correct lateral deflections of the boom tip via cables loaded under tension that is assumed to connect from the tip of the spreader bar to the tip of the boom. Design B notably does not include the spreader bars or the cables. The primary objective of this study is to determine if and where the cable-stayed design exhibits superior performance in the design space and quantify this advantage.

The lunar tower designs are shown in Fig. 2 in their initial states with only the lateral eccentricity and their final deflected states when compression is accounted for due to the tip mass and boom self-weight. The design variables considered in this study are also shown in the figure. They are the boom length, $L$, tip payload mass, $M$, initial eccentricity, $e$, flexural stiffness, $EI$, cable tension, $T$, and cable angle relative to the vertical axis, $\alpha$, which is itself a function of boom tip displacement, $w(L)$, spreader bar length, $S$, and $L$. A top down view of the cable-stayed design A is shown in Fig. 3 with tip deflection defined by the initial eccentricity and direction $\theta$.

Several assumptions are made to both simplify analysis and serve to probe the structural design space. Firstly, the proposed deployment mechanism results in the COROTUB not fully deploying near the base as shown in Fig. 1, so there is steady variation in its cross-sectional profile. Therefore, its flexural stiffness $EI$ would more accurately be a function of $x$, which is the coordinate along the longitudinal axis of the boom. This dependence of $EI$ on $x$ is because the boom transition length from the flattened coiled state to the fully deployed state is longer than the base deployer mechanism. The boom exits the mechanism with a partially deployed cross-section that continues to develop beyond the mechanism where the plug is located. Since the plug shown in Fig. 1(c) is fixed relative to the deployer frame and the hub, the COROTUB is assumed to be cantilevered from the plug position. The cables are assumed to be inextensional, but their lengths adjust with lateral tower deflection while constant tension is being applied from the motorized spools located in the base [1]. The spreader bars are rigid and they are equally spaced around the boom. Finally, small deflections and

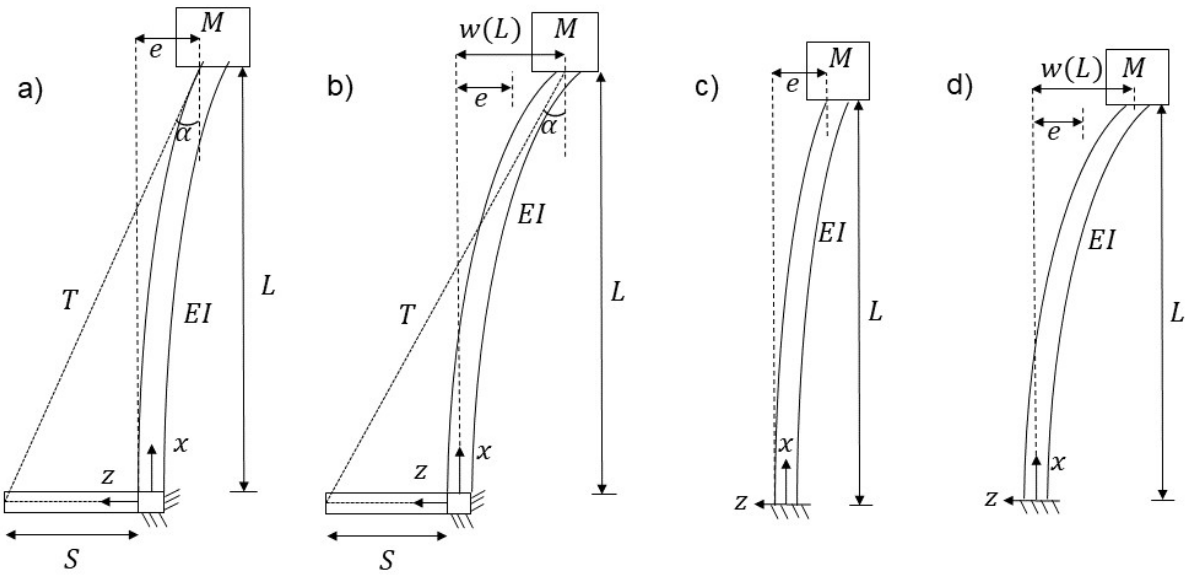


**Fig. 2 Lunar tower designs. (a) Design A with initial eccentricity and (b) at final displacement due to tip mass and tensioned cable. (c) Design B with initial eccentricity, and (d) at final displacement due to tip mass.**

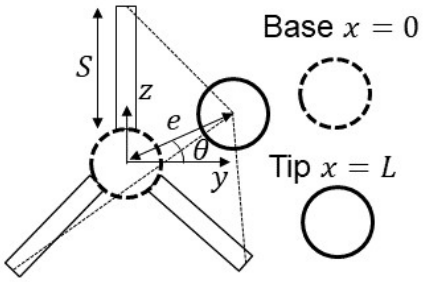


**Fig. 3 Top down view of the lunar tower design A showing the tip deflection defined by eccentricity, $e$, at an angle from the y-axis $\theta$.**

rotations are assumed throughout the analysis.

The lunar towers are analyzed as fixed-free beam-columns subject to lateral bending from the eccentricity and compressive loading, $P$, from the tip mass and the self-weight of the boom. Since the beam-column inherently exhibits axial curvature from being imperfection sensitive, any compressive loading will further exacerbate its lateral deflection. This growth in deflection is asymptotically unbounded as $P$ approaches the Euler buckling load, $P_{cr}$, as given by:

$$P_{cr} = \frac{\pi^2 EI}{4L^2} \tag{1}$$

Note that Eq. 1 only applies when $EI$ is constant. As discussed previously, there exists a region along the COROTUB base where its cross-sectional profile, and by extension the second moment of area $I$, is not constant. This effect is explored in the following sections. Since $P$ will never reach $P_{cr}$, the limiting condition of the tower design is excessive deflection as local shell buckling and material failure are not considered in this paper. Alternatively, critical deflection limits, which cause either of the two failure modes, could be imposed since the boom properties are assumed to be identical between designs A and B.

### A. COROTUB Profile

The deployment mechanism shown in Fig. 1 results in a deployed cross-section that varies with length along the boom's longitudinal axis $x$. The second moments of area are thus $I_{yy}(x)$ and $I_{zz}(x)$ and it is necessary to account for their distribution in the analytical model. To that end, a finite element model of a candidate COROTUB with a length of 16.5 m and flattened height of 325 mm was analyzed in Abaqus/Standard* to predict the geometry when constrained within the deployer. The boom plug shown in Fig. 1 (c) is 2.2 m above the hub where the boom is flattened. Since the plug enforces a cross-section that is more narrow than the manufactured shape, there exists a transition length, $L_T$, above the plug which the boom recovers its natural geometry. Taking the fixed plug end as $x = 0$ m, the recovered geometry is found to begin at approximately $L_T = 3$ m. The nodal coordinates across this transition length are used to calculate $I_{yy}(x)$ and $I_{zz}(x)$. The cross-section above $L_T$ is assumed to be constant and approximated by the shape at $x = 3$ m.

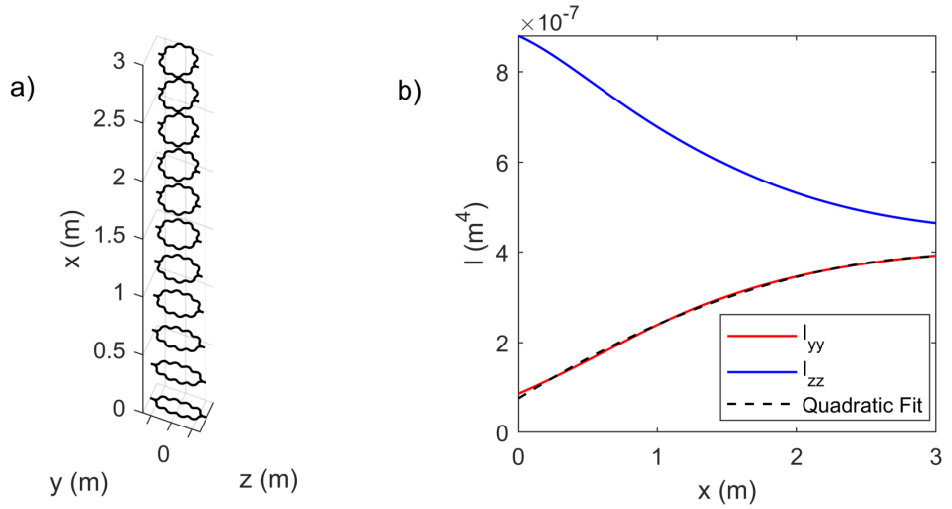


**Fig. 4 (a) COROTUB cross-section from the plug ($x = 0$ m) to the nominal shape ($x = 3$ m) with profiles shown in 0.3 m increments. (b) Corresponding second moments of area $I_{yy}$, $I_{zz}$, and the quadratic fit used for $I_{yy}$ as a function of $x$.**

The nodal coordinates of the COROTUB cross-section are plotted in Fig. 4 (a) in 0.3 m increments to illustrate the profile variation. Note that the actual nodal increment in finite element model is 0.01 m. The corresponding second moments of area are shown in Fig. 4 (b) and these are estimated with the numerical procedure outlined in [3, 4]. Since the aim is to find the most conservative allowable tip mass under the worst case loading conditions, the lower of the two parameters, or $I(x) = min\{I_{yy}(x), I_{zz}(x)\}$, is evaluated for subsequent analysis. A least squares fit of $I_{yy}(x)$ to a quadratic function is obtained to enable the analytical derivation of relevant metrics such as the boom buckling load and deflection. The symbolic equation is given by:

$$I(x) = \begin{cases} c_1 x^2 + c_2 x + c_3 & 0 \le x \le L_T \\ I_0 & L_T \le x \le L \end{cases} \tag{2}$$

where the piecewise form separates the cross-sectional transition region from the rest of the boom. Note that higher-ordered polynomials provide $I_{yy}(x)$ fits with even greater accuracy, but they become increasingly difficult to analytically derive and computationally expensive to evaluate when integrated into the metrics of interest. The numerical equation evaluated for the COROTUB is given by:

$$I(x) = \begin{cases} -2.937 \times 10^{-8} x^2 + 1.932 \times 10^{-7} x + 7.572 \times 10^{-8} \text{m}^4 & 0 \le x \le 3\,\text{m} \\ 3.918 \times 10^{-7}\,\text{m}^4 & x \ge 3\,\text{m} \end{cases} \tag{3}$$

*Specific vendor and manufacturer names are explicitly mentioned only to accurately describe the material or test hardware. The use of vendor and manufacturer names does not imply an endorsement by the National Aeronautics and Space Administration (NASA) nor does it imply that the specified material or equipment is the best available.

### B. Euler Buckling Load

The COROTUB deployment mechanism results in a non-uniform cross-section along the length of the boom, therefore Eq. 1 does not apply. Instead, the Rayleigh-Ritz method is used to approximate the buckling loads, $P_n$, and buckling modes, $\Phi_n$. These may be considered to be eigenloads and eigenmodes of the system, respectively. Therefore let the $n$th eigenmode be defined as:

$$\Phi_n(x) = \sum_{i=1}^{N} q_i^{(n)} \psi_i(x) \tag{4}$$

where $N$ denotes the number of eigenmodes to be approximated by this method. As $N$ increases, the $P_n$ and $\Phi_n$ approximations converge to the exact solution, but their computations also become increasingly costly. For the COROTUB, a convergence study was performed and $N = 4$ was deemed to be both sufficiently accurate and numerically manageable. $q_i^{(n)}$ represents the $n$th set of unknown constants and $\psi_i(x)$ is the arbitrary shape function with dependence on $x$.

The shape functions must fulfill two criteria to be admissible: they must be differentiable half as many times as the order of the system (i.e. twice differentiable) and they must satisfy only the geometric boundary conditions. As such, a suitable set of shape functions for a fixed-free boom is chosen to be:

$$\psi_i(x) = x^{i+1} \tag{5}$$

At the point of instability, the second variation of the potential energy of the boom along the pre-buckled configuration (i.e. principal branch) is zero, or $\delta^2 U = 0$. Buckling loads are approximated by using admissible guesses with $\psi_i(x)$ for the buckled deflection. The Rayleigh-Ritz formulation leads to the following system described in terms of the unknown constants $\{q\}$:

$$[K]\{q\} = 0 \tag{6}$$

where $[K]$ is the $N \times N$ stiffness matrix of the boom. As shown in Eq. 7, $K_{ij}$ is the definition of each element in $[K]$ and it is a function of the axially compressive load, $P$, at the tip, $L$, $EI(x)$, and $\psi_i(x)$.

$$K_{ij} = \int_0^L \left( EI(x) \frac{d^2\psi_i}{dx^2} \frac{d^2\psi_j}{dx^2} - P \frac{d\psi_i}{dx} \frac{d\psi_j}{dx} \right) dx \tag{7}$$

Since the variance of $I(x)$ is known to only persist in the region $0 \leq x \leq L_T$, the first term of the integral in Eq. 7 may be divided into two regions as follows:

$$K_{ij} = \int_0^{L_T} \left( EI(x) \frac{d^2\psi_i}{dx^2} \frac{d^2\psi_j}{dx^2} \right) dx + \int_{L_T}^{L} \left( EI_0 \frac{d^2\psi_i}{dx^2} \frac{d^2\psi_j}{dx^2} \right) dx - \int_0^{L} \left( P \frac{d\psi_i}{dx} \frac{d\psi_j}{dx} \right) dx \tag{8}$$

A non-trivial solution for $\{q\}$ requires that the stiffness matrix $[K]$ be singular, or

$$\det[K] = 0 \tag{9}$$

Evaluating Eq. 9 yields the characteristic equation of the system. Its roots are the buckling loads, $P_n$, and the minimum of these gives the critical buckling load of the boom, $P_{cr}$. By finding the corresponding eigenvectors, $q^{(n)}$, the buckling modes can be computed through Eq. 4.

### C. Unsupported Reference Tower Design

The allowable payload tip mass that can be carried by the reference tower design B is derived in this section. The exact initial profile of the deployed booms due to the eccentricity is unknown, so the initial shape, $w(x)$, is assumed to be the first buckling mode of a fixed-free column, defined as:

$$w(x) = -e \left( 1 - \cos \frac{\pi x}{2L} \right) \tag{10}$$

where the eccentricity, $e$, sets the amplitude of the mode. The total deflection of the boom is then found by applying the amplification factor, $\frac{1}{1-\frac{P}{P_{cr}}}$, onto Eq. 10, which accounts for additional deflection caused by axial compression, $P$ [19]. The deflection is thus given by:

$$w(x) = -\frac{e}{1-\frac{P}{P_{cr}}}\left(1-\cos\frac{\pi x}{2L}\right) \tag{11}$$

Eq. 11 remains a simple and accurate approximation for the beam-column deflection when $P << P_{cr}$. The axial compression due to the total weight of the tip mass, $M$, and the boom itself is expressed as:

$$P = Mg + \frac{3}{10}\rho g L \tag{12}$$

where $g$ is the gravitational acceleration on the celestial body ($g = 1.625\,\mathrm{m/s^2}$ on the lunar surface), $\rho$, is the the boom linear mass density, and the self-weight of the boom is approximated as a tip load with a $\frac{3}{10}$ factor [19]. Substituting Eq. 12 into Eq. 11 that is evaluated at $x = L$ gives an expression for the boom tip deflection:

$$w(L) = \frac{-e}{1-\frac{1}{P_{cr}}(Mg+\frac{3}{10}\rho g L)} \tag{13}$$

The primary performance metric when comparing the two designs is chosen to be the supported tip mass, $M$. Solving Eq. 13 for $M$ yields:

$$M_B = \frac{P_{cr}}{g}\left(\frac{e}{w(L)}+1\right) - \frac{3}{10}\rho L \tag{14}$$

where this equation represents the allowable tip mass for the reference tower design B, $M_B$, when the allowable maximum tip deflection, $w(L)$, is specified. Note that $P_{cr}$ corresponds to that of the non-uniform COROTUB profile as found in the previous section.

### D. Cable-stayed Primary Tower Design

The primary design A is identical to reference design B with the exception of the added spreader bars and tensioned guy wires as shown in Fig. 2. Before the allowable tip mass can be derived for comparison against the reference tower design, its possible states of deflection must be formally defined. It is convenient to first define the general deflection of the tip mass in cylindrical coordinates to illustrate radial symmetries inherent to the system. Note that all deflections are assumed to be sufficiently small such that the length of the boom is approximately unchanged. The three spreader bars are equally spaced radially and located at the fixed end of the tower (i.e. $x = 0$). Due to the small deflections assumption, only the radial coordinates $(r, \theta)$ need be considered, and they dictate the Cartesian displacement as follows:

$$r = w(L) \tag{15a}$$

$$y = r\sin\theta \tag{15b}$$

$$z = r\cos\theta \tag{15c}$$

For all deflection directions $\theta$, it can be shown that there are at most two cables that provide a useful corrective force. That is, there only exist deflections where one or two cables have tension components that lie in the direction of the origin. Therefore, the total correction of the tip mass deflection must be due to at most two tension forces, $T_1$ and $T_2$. The convention is chosen such that $T_1$ corresponds to the longer of the two cables and $T_2$ corresponds to the shorter.

The radial symmetry of the system, divided into six regions by the three spreader bars and projected at $x = 0$, is illustrated by Fig. 5, along with two simplifying cases that arise from the boundaries of these regions. In case 1, shown in Fig. 5(b), the tip mass is deflected directly opposite one spreader bar. In this case, only one cable contributes a useful corrective force, as any tension on the other two cables would serve to increase deflection away from the origin. Therefore cable tensions are $T_1 \neq 0$ and $T_2 = 0$. In case 2, shown in Fig. 5(c), deflection is directly along one spreader bar and $T_1 = T_2$.

For this analysis, case 1 may be explicitly defined as $\theta = \{30°, 150°, 270°\}$ and case 2 as $\theta = \{90°, 210°, 330°\}$. For all other $\theta$, the cables corresponding to $T_1$ and $T_2$ in each region are summarized in Table 1. The radial symmetries

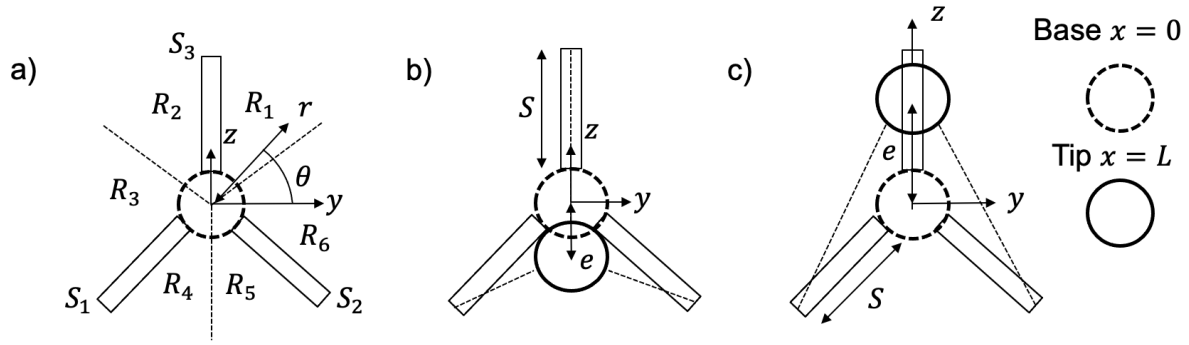


**Fig. 5 Top-down projection of possible tip mass deflections. (a) Regions of radial symmetry - deflection orientation described by $\theta$. (b) Case 1 - deflection is directly opposite one spreader bar. (c) Case 2 - deflection is directly along one spreader bar.**

allow the analysis of a single region to be mirrored to all other regions, and it is chosen to be $R_1$ as bounded between 30° and 90°. In the following sections, it will be shown that the deflection within the regions may be expressed as a function of $T_1$ only, where $T_2$ depends on $T_1$.

**Table 1 Regions of radial symmetry and corresponding cable assignments.**

| Tip Mass Region | Long Cable, $T_1$ | Short Cable, $T_2$ | $\theta$ Range |
|---|---|---|---|
| $R_1$ | $S_1$ | $S_2$ | $30° < \theta < 90°$ |
| $R_2$ | $S_2$ | $S_1$ | $90° < \theta < 150°$ |
| $R_3$ | $S_2$ | $S_3$ | $150° < \theta < 210°$ |
| $R_4$ | $S_3$ | $S_2$ | $210° < \theta < 270°$ |
| $R_5$ | $S_3$ | $S_1$ | $270° < \theta < 330°$ |
| $R_6$ | $S_1$ | $S_3$ | $330° < \theta < 30°$ |

*1. Horizontal and Vertical Cable Tension Components*

As before, compressive loading on a fixed-free beam-column with initial eccentricity will have excessive deflection as its design limiting condition. The three spreader bars each connect via a cable to the tip of the boom, offering some mitigation to deflection due to their combined horizontal component, $T_h$, of the total tension, $T$. However, this tension also includes a vertical component, $T_x$, as a compressive force on the boom, which further exacerbates deflection. Therefore, the tension must be carefully specified as to maximize $T_h$ and minimize $T_x$ given a set of spreader bar and boom lengths.

Consider a deflection of the tip mass that falls into region $R_1$ with arbitrary direction $\theta$. The long cable, and therefore $T_1$, originates from $S_1$. An illustration of the cable and the angles used to decompose $T_1$ into $x$, $y$, and $z$ components is shown in Fig. 6. The angle $\beta_1$ and horizontal component of cable length $C_1$ are in the horizontal plane at $x = 0$, and cable angle $\alpha_1$ is respect to vertical axis $x$. The quantities $\beta_1$, $C_1$, and $\alpha_1$ are defined from Fig. 6 as:

$$\beta_1 = \tan^{-1}\left(\frac{(\sqrt{3}/2)S + y}{S/2 + z}\right) \tag{16a}$$

$$C_1 = \sqrt{\left(\frac{\sqrt{3}}{2}S + y\right)^2 + \left(\frac{S}{2} + z\right)^2} \tag{16b}$$

$$\alpha_1 = \tan^{-1}\left(\frac{C_1}{L}\right) \tag{16c}$$

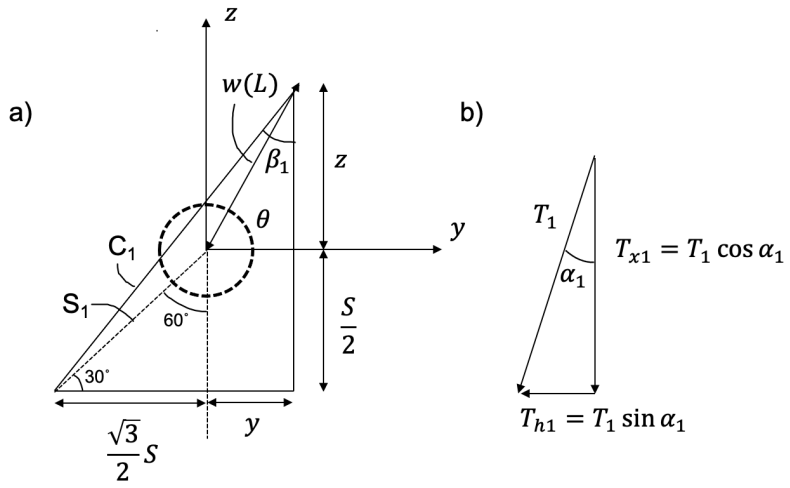


**Fig. 6 (a) Projection of long cable with $T_1$ onto horizontal plane at $x = 0$ for deflection in region 1. (b) Long cable horizontal and vertical tension components.**

The shorter cable originates from the spreader bar $S_2$ with tension, $T_2$. Its projection along with the tension components are shown in Fig. 7.

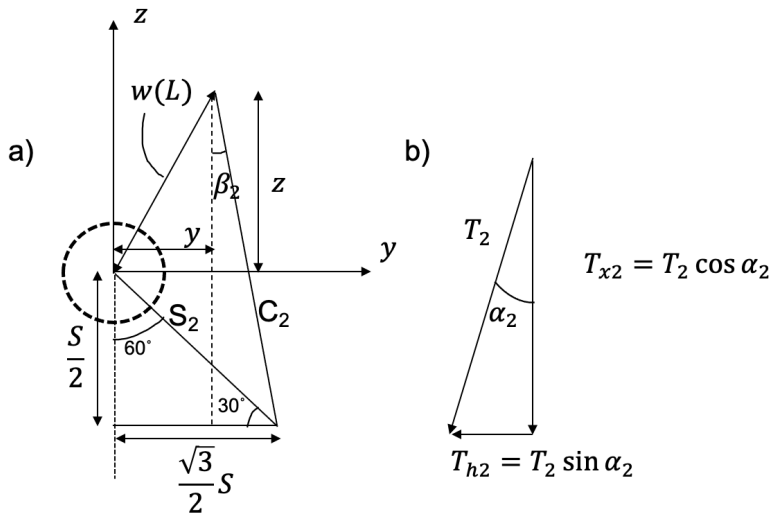


**Fig. 7 (a) Projection of short cable with $T_2$ onto horizontal plane at $x = 0$ for deflection in region 1. (b) Short cable horizontal and vertical tension components.**

The corresponding angles and lengths are similarly defined as:

$$\beta_2 = \tan^{-1}\left(\frac{(\sqrt{3}/2)S - y}{S/2 + z}\right) \tag{17a}$$

$$C_2 = \sqrt{\left(\frac{\sqrt{3}}{2}S - y\right)^2 + \left(\frac{S}{2} + z\right)^2} \tag{17b}$$

$$\alpha_2 = \tan^{-1}\left(\frac{C_2}{L}\right) \tag{17c}$$

As shown in Fig. 6(b) and 7(b), $T_1$ and $T_2$ are divided into vertical, $x$, and horizontal, $h$, components. The latter is then further divided into $y$ and $z$ components using Eqs. 16a-17c:

$$T_{x1} = T_1 \cos\alpha_1 \tag{18a}$$

$$T_{h1} = T_1 \sin\alpha_1 \tag{18b}$$

$$T_{z1} = T_{h1} \cos\beta_1 \tag{18c}$$

$$T_{y1} = T_{h1} \sin\beta_1 \tag{18d}$$

The components of $T_2$ are similarly defined as above with the subscript 2, and the vector sum of the horizontal $z$ and $y$ components gives the total corrective force. For the resultant corrective force to be oriented back to the origin, the total vector sum of $y$ and $z$ components must lie along the direction $\theta$ with opposite magnitude, therefore:

$$\theta = \tan^{-1}\left(\frac{T_{hz}}{T_{hy}}\right) = \tan^{-1}\left(\frac{T_1 \sin\alpha_1 \cos\beta_1 + T_2 \sin\alpha_2 \cos\beta_2}{T_1 \sin\alpha_1 \sin\beta_1 - T_2 \sin\alpha_2 \sin\beta_2}\right) \tag{19}$$

where $T_{hz} = T_{z1} + T_{z2}$ and $T_{hy} = T_{y1} + T_{y2}$. Eq. 19 can then be solved for $T_2$ as a function of $T_1$:

$$T_2 = \frac{-T_1 \cos(\beta_1 + \theta) \sin\alpha_1}{\sin\alpha_2 \cos(\beta_2 - \theta)} \tag{20}$$

Evaluating Eq. 20 reveals that given $\theta$, $T_2$ becomes linear with respect to $T_1$. If $\theta = 30°$, then $T_1 \neq 0$ and $T_2 = 0$ as predicted in case 1. If $\theta = 90°$, then $T_2 = T_1$ and case 2 is recovered. For $30° < \theta < 90°$, $T_2 < T_1$ will always hold, so practical limits on the cable tension will always be dictated by the longer cable with $T_1$. Substituting Eq. 20 into the total vertical force $T_x = T_{x1} + T_{x2}$ and total horizontal force $T_h = T_{h1} + T_{h2}$ will enforce the orientation condition on the resultant corrective force while keeping the equations in terms of $T_1$. These are given by:

$$T_x = T_1 \cos\alpha_1 - \frac{T_1 \cos(\beta_1 + \theta) \sin\alpha_1 \cos\alpha_2}{\sin\alpha_2 \cos(\beta_2 - \theta)} \tag{21}$$

$$T_h = \sqrt{\frac{T_1^2(\cos(2\alpha_1) - 1)(\cos(2\beta_1 + 2\beta_2) - 1)}{2(\cos(2\beta_2 - 2\theta) + 1)}} \tag{22}$$

*2. Allowable Tip Mass*

To find the allowable tip mass, the total deflection of the cantilevered boom must first be defined as:

$$w(x) = \frac{-e}{1 - \frac{P+T_x}{P_{cr}}}\left(1 - \cos\frac{\pi x}{2L}\right) + w_c(x) \tag{23}$$

where the first two terms are the beam-column eccentricity amplified by the compression due to the total weight $P$ and cable force $T_x$. These retain the same form as Eq. 11 and are superposed to $w_c(x)$, which describes the corrective beam deflection due to the lateral tip load that is caused by $T_h$. This deflection equation may be derived from the beam moment equation $M(x)$ given below:

$$M(x) = \begin{cases} EI(x)\frac{d^2w_c}{dx^2} = T_h(L - x) & 0 \le x \le L_T \\ \\ EI_0\frac{d^2w_c}{dx^2} = T_h(L - x) & L_T \le x \le L \end{cases} \tag{24}$$

where the piecewise form is due to the dependence on $I(x)$ given in Eq. 2. The piecewise $w_c(x)$ is found by integrating Eq. 24 twice and applying the following boundary and matching conditions:

$$w_c(0) = 0 \tag{25a}$$

$$\frac{dw_c}{dx}(0) = 0 \tag{25b}$$

$$w_c^-(L_T) = w_c^+(L_T) \tag{25c}$$

$$\frac{dw_c^-}{dx}(L_T) = \frac{dw_c^+}{dx}(L_T) \tag{25d}$$

where the superscripts − and + refer to the $0 \leq x \leq L_T$ and $L_T \leq x \leq L$ ranges, respectively. Evaluating Eq. 23 at the boom tip, $x = L$, after substituting in $P$ from Eq. 12 yields:

$$w(L) = \frac{-e}{1 - \frac{1}{P_{cr}}(T_x + Mg + \frac{3}{10}\rho g L)} + w_c(L) \tag{26}$$

where $w_c(L)$ is from the deflection equation corresponding to $L_T \leq x \leq L$. Again, the expression for tip mass as a function of maximum tip deflection, and in this case, cable tension, is sought. Solving Eq. 26 for $M$ gives:

$$M_A = \frac{P_{cr}}{g}\left(\frac{e}{w(L) - w_c(L)} + 1\right) - \frac{T_x}{g} - \frac{3}{10}\rho L \tag{27}$$

where $M_A$ is the allowable tip mass for the cable-stayed tower design A. Note that while the full definitions for Eqs. 14 and 27 are not shown due to excessive complexity, the analytical framework presented in this section lets the allowable tip mass to be compared between architectures as a function of $L$, and for design A: $\theta$, $S$, and $T_1$. This comparison forms the basis of the analysis presented in the next section.

## III. Parametric Analysis

### A. Design Parameters

The targeted comparison between the two proposed designs is the allowable tip mass, $M$, while assuming identical parameters in boom length, $L$, flexural stiffness, $EI(x)$, linear mass density, $\rho$, maximum allowable tip deflection, $w(L)$, and initial eccentricity, $e$. Note that, where appropriate, subscripts A and B will be used to refer to properties of a specific design. In reference to sizing requirements for SELTI, boom lengths of 5 m to 30 m are being considered. The excessive deflection limit is chosen as $w(L) = -w_{lim}L = -0.03L$, or 3% of the boom length. The initial eccentricity due to stowage-induced creep, manufacturing imperfections, thermal loading, and a 1° base tilt is assumed to be $e = e_{max}L = 0.0275L$, or 2.75% of the boom length. As shown in Fig. 3, it is assumed that the eccentricity due to these factors are aligned in the same direction for conservatism.

The spreader bar length, $S$, is normalized with respect to the boom length such that $\hat{S} = S/L$, and a $\hat{S} \leq 0.2$ limit is imposed to be aligned with SELTI system requirements. Note that $\hat{S}$ is used to more clearly illustrate the relationship between spreader bar length and all investigated boom lengths. As described in Table 1, the deflection direction $\theta$ is considered to be within region $R_1$. Note that the longer cable tension, $T_1$, is still a design parameter, but no specific range is imposed. The effective elastic modulus, $E$, of the COROTUB laminate is approximated as 80.7 GPa when coupled with $I_{yy}(x)$. The material properties and design parameters to be used in the results are given in Table 2.

**Table 2 Material Properties and Design Parameters.**

| Property | Symbol | Value(s) | Units |
|---|---|---|---|
| Boom Length | $L$ | 5 to 30 | m |
| Boom Deflection Limit | $w_{lim}$ | 0.03 | None |
| Boom Max Eccentricity | $e_{max}$ | 0.0275 | None |
| Boom Linear Mass Density | $\rho$ | 0.15 | kg/m |
| Boom Elastic Modulus | $E$ | 80.7 | GPa |
| Boom Deflection Direction | $\theta$ | 30 to 90 | ° |
| Normalized Spreader Bar Length | $\hat{S}$ | 0 to 0.2 | None |

**B. Optimization of Allowable Tip Mass**

Using the parameters defined in Table 2, a comparison of the allowable tip mass between designs A and B is carried out to determine the efficacy of each design. For an initial comparison, the spreader bar length is set to $S = 1.5$ m and the longer cable tension is $T_1 = 10$ N. These properties are considered representative of the hardware prototypes of SELTI. A comparison between $M_A$ and $M_B$ as a function of the boom length is shown in Fig. 8(a) and the ratio $\frac{M_A}{M_B}$ to quantify the difference is provided in Fig. 8(b). The deflection direction is set to case 1, or $\theta = 30°$.

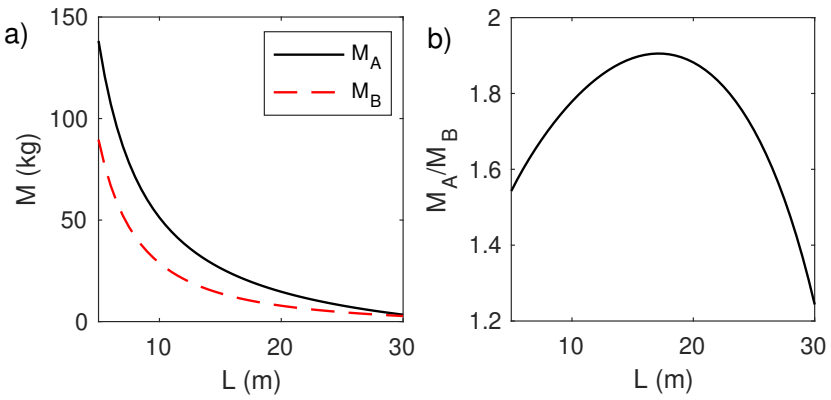


**Fig. 8 (a) Initial comparison of allowable payload tip mass between designs A and B and (b) their ratio as a function of boom length, $L$.**

The cabled-stayed design A outperforms the unsupported design B across the entire range of investigated boom lengths due to being stabilized by the spreader bar and the tensioned cable. This result shows that the deflection of design A being negated by the cable tension directly translates to a larger allowable tip mass when compared to design B. For all boom lengths, design A is found to support over 1.2 times the mass of design B. The largest margin is found at $L = 17$ m where $\frac{M_A}{M_B} = 1.9$. Above this length, the benefit of the spreader bar begins to diminish as the cable angle relative to the boom, $\alpha$, decreases to a point where the compressive load, $T_x$, of the tensioned cable exacerbates the total deflection more than being negated by the corrective load, $T_h$.

To fully evaluate the merits of the cable-stayed design A, its optimal parameters are first determined before comparing against reference design B. Maximizing the allowable tip load on design A involves considering the normalized spreader bar length and cable tension as free parameters. To accomplish this, the parameter space is first explored in Fig. 9 which shows the allowable tip mass, $M_A$, as functions of $\hat{S}$ and $T_1$ at a fixed boom length of $L = 15$ m. Specifically, the plots correspond to $\theta$ of (a) 30°, (b) 50°, (c) 70°, and (d) 90° to illustrate the performance variation with respect to the deflection direction. These values of $\theta$ represent a sampling of the entire region $R_1$ examined in this analysis.

Considering Eqs. 16 and 17, it becomes apparent that increasing the spreader bar length will increase $\alpha$, lowering the compressive load on the boom and increasing the lateral tip load. The increased lateral tip load reduces the boom tip deflection and ultimately increases $M_A$. This trend is observed in Fig. 9 for all deflection directions where $M_A$ increases with $\hat{S}$. However in practice, increasing spreader bar length will impart a penalty on the overall system mass, complexity, and retains an upper limit.

When considering the cable tension $T_1$, a local optimum which maximizes $M_A$ is revealed in the contour plots and these are illustrated by the red lines as functions of $\hat{S}$. The optimum indicates the ratio of $T_x$ to $T_h$ such that total deflection is minimized. Interestingly, there exists a small range of very low spreader bar lengths where the optimal tension is zero, implying that any cable tension is detrimental to the load carrying capacity of the cable-stayed tower. Contrary to $\hat{S}$, controlling the cable tension do not induce a system mass penalty and therefore the optimum tension should be exploited. If the deflection direction is considered, $\theta = 30°$ (i.e. case 1) yields the largest allowable tip mass and this performance decreases to the lowest allowable tip mass at $\theta = 90°$, or case 2. These trends are found to be consistent across the boom length range of interest.

To evaluate the cable-stayed design A with optimal performance, the optimal tension that maximizes $M_A$ is found by

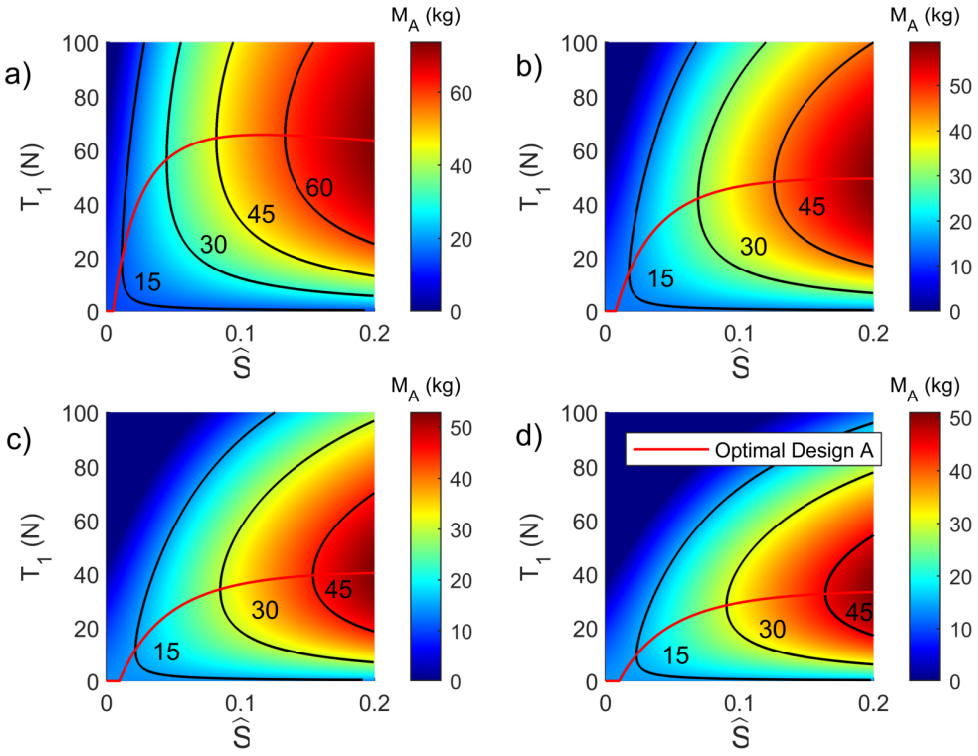


**Fig. 9 Allowable tip mass, $M_A$, as a function of the cable tension, $T_1$, and normalized spreader bar length, $\hat{S}$, when $L = 15$ m. Deflection directions are (a) $\theta = 30°$, (b) $\theta = 50°$, (c) $\theta = 70°$, and (d) $\theta = 90°$. Black contour lines trace $M_A$ values in increments of 15 kg.**

substituting Eqs. 21 and 22 into Eq. 27, differentiating it with respect to $T_1$, and then setting it equal to zero as shown below:

$$\frac{\partial M_A}{\partial T_1} = 0 \tag{28}$$

Then the optimized $T_1$ is solved from Eq. 28 which maximizes $M_A$ by satisfying the condition $\frac{\partial^2 M_A}{\partial T^2} < 0$. Due to the complexity of the optimal $T_1$ equation, it is always computed numerically. The red lines shown in Fig. 9 are found to match the evaluated optimal tension, except for low values of $\hat{S}$ where optimal tension is found to be negative (where the red lines have $T_1 = 0$). Since negative tension is unrealistic for the cables, the optimal tension is set to zero. Note that the shorter cable tension $T_2$ is also zero if $T_1 = 0$ from Eq. 20. This fact means that designs A and B will have identical allowable tip mass for these $\hat{S}$ ranges since the cables contribute no useful load. As shown in Fig. 9, this $\hat{S}$ transition point where the optimal tension turns to zero is found to increase as $\theta$ also increases from 30° to 90°. Substituting the optimized tension $T_1$ back into Eq. 27 will formally yield the maximized allowable tip mass for the cable-stayed design A.

### C. Performance Comparison

For a full performance comparison, $M_B$ in Eq. 14 and the maximized $M_A$ with the optimal cable tensions are evaluated for the full range of $L$ and $\hat{S}$ and results are shown in Fig. 10. Specifically, Fig. 10(a) and (d) show $max\{M_A, M_B\}$, or the maximum of the allowable tip masses between designs A and B. The allowable tip mass ratio $\frac{M_A}{M_B}$ are shown in Fig. 10(b) and (e) and the corresponding optimal tension, $T_1$, for the cable-stayed design are shown in Fig. 10(c) and (f). The deflection direction of $\theta = 30°$ is shown in Figs. 10(a) through (c) and for $\theta = 90°$ in Figs. 10(d) through (f). The black contour lines trace specific metric values relative to the varying parameters. The red line is the

boundary that delineates the regions where designs A and B are the better performing architecture. This boundary corresponds to the critical $\hat{S}$ values where the optimal tension of design A becomes zero per length and deflection direction. Thus, $M_A > M_B$ in the region above the boundary line and $M_A = M_B$ in the region below it.

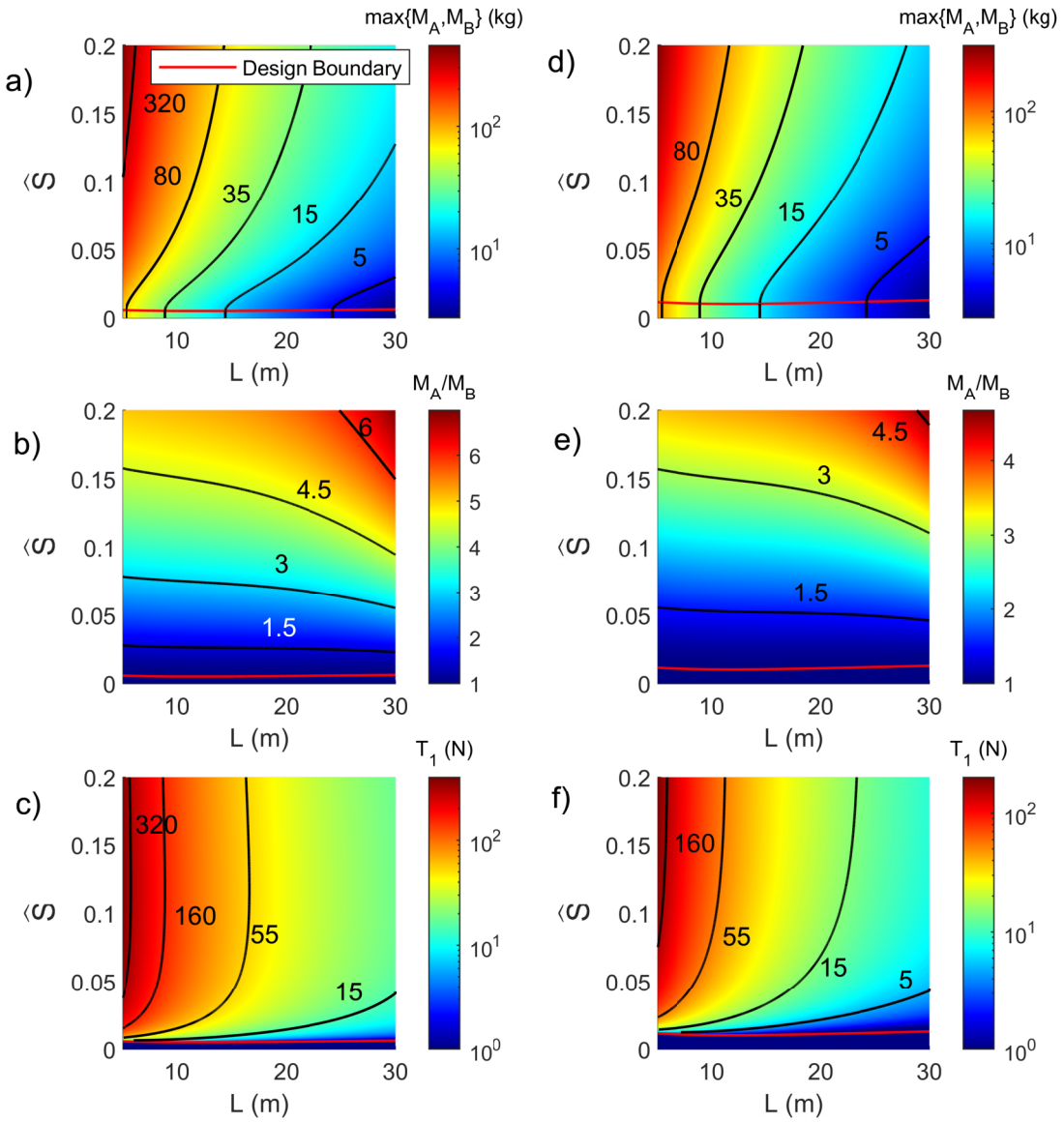


**Fig. 10 Optimized allowable tip mass shown as (a) the maximum of designs A and B, (b) the ratio $\frac{M_A}{M_B}$, and (c) the design A's corresponding optimal tension $T_1$ as functions of the boom length $L$, and normalized spreader bar length, $\hat{S}$, for $\theta = 30°$. (d)-(f) are analogous to (a)-(c) except that $\theta = 90°$. $M_A > M_B$ and $M_A = M_B$ above and below the red line, respectively.**

It is observed that design A outperforms design B for the majority of the investigated range of boom and spreader bar lengths as well as the deflection directions. As expected, the margin by which design A outperforms B increases as the spreader bar is lengthened while the boom length is shortened due to directly increasing the cable angles with

respect to the vertical boom axis, $\alpha$. As $\alpha$ increases, the total compressive load, $T_x$, on the boom decreases while the corrective load, $T_h$, increases when reacted from the optimized cable tension. Therefore, for any given length requirement, maximizing the spreader bar length is critical for achieving favorable load carrying performance.

While allowable tip mass may be identical below the design boundary, the increased mass and implementation complexity of the spreader bar system, which adds no benefit in this range due to zero cable tensions, makes design B preferred over design A. However, this represents a minimal portion of the design space where the spreader bar length is extremely small relative to the tower height. The optimal tension, $T_1$, for the longer cable increases with $\hat{S}$ and decreases with $L$ in the region of the parameter space where $M_A > M_B$, and remains as zero when $M_A = M_B$. This correlation reveals that the upper cable tension requirement will generally scale with the allowable tip mass for design A since $T_1 \geq T_2$ across the entire parameter space. A useful guide to what the design restrictions are if an upper limit on the cable tension is specified for the tower system is provided in Fig. 10(c), as the $\theta = 30°$ case requires the largest tensile loads for the longer cable.

When the deflection directions are compared, the $\theta = 90°$ case is most detrimental to the allowable tip mass while the $\theta = 30°$ case is the most favorable for the cable-stayed design A. While the intermediate angles are not shown, the corresponding $M_A$ values scale from their minimum at $\theta = 90°$ to their maximum at $\theta = 30°$, which follows the trends seen in Fig. 9. This correlation indicates that if the boom eccentricity is oriented such that the shorter cable has less influence, then the tower will be able to carry larger tip masses. The worst loading case would then be if the eccentricity is aligned with any of the three spreader bars as this deflection would require equal cable tension from the remaining two bars. Another observation is that the design boundary has larger $\hat{S}$ values as $\theta$ increases to 90°, which means that the cable-stayed design A is less favorable over the design space.

To further reveal why $\theta = 90°$ is the worst deflection direction for $M_A$, comparisons are made for the total compressive $T_x$ and corrective $T_h$ forces due to the cable tensions between the worst $\theta = 90°$ and best $\theta = 30°$ cases. This is expressed in terms of their ratio $T^{90°}/T^{30°}$ vs. $\hat{S}$ at $L = 15$ m and are shown in Fig. 11. It is observed that the $\theta = 90°$ case induces relatively larger total compressive force $T_x$ than the total corrective force $T_h$ when compared against the $\theta = 30°$ case. Therefore, the induced deflection due to the cable tensions outpaces their corrective influence and imposes a harsher penalty on the allowable tip mass $M_A$. This trend is exacerbated as the spreader bar length is increased which worsens the disparity between the two extreme loading cases. This finding is found to be consistent across all values of boom length, $L$.

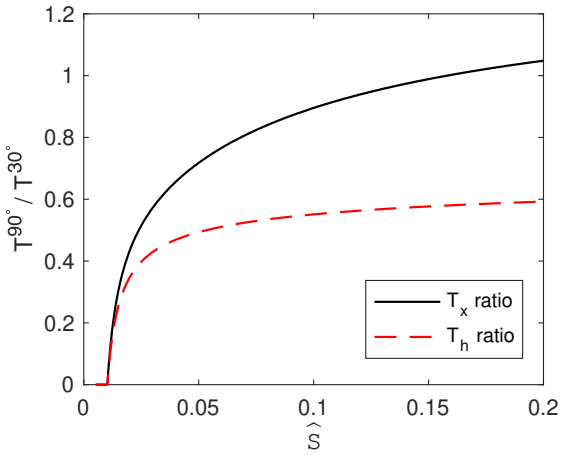


**Fig. 11 Ratios for the total compressive and corrective, $T_x$ and $T_h$, respectively, loads due to cable tensions between $\theta = 90°$ and $\theta = 30°$ as functions of $\hat{S}$ at $L = 15$ m.**

## IV. Lunar Towers with CTM Booms

The analytical framework is used to compare the allowable tip mass of lunar tower designs A and B utilizing the CTM composite booms as the load carrying structure. Its nominal cross-section is shown in Fig. 12 and it is relatively smaller than that of the COROTUB with a flattened height of 145 mm.

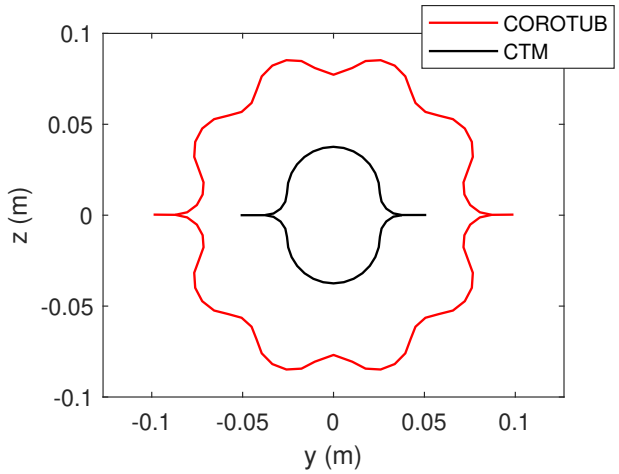


**Fig. 12 Cross-section of CTM boom at plug location. Plug cross-section is the same as the nominal cross-section. Fully deployed COROTUB profile from Fig. 4(a) shown for comparison.**

Unlike the COROTUB and its deployer mechanism, the CTM version of SELTI has an exit plug that retains the fully deployed cross-sectional shape shown in Fig. 12. Therefore, it is assumed that the CTM cross-section is uniform and its flexural stiffness, $EI$, is constant. The lower of the two directional second moment of areas is still $I_{yy}$ and this value is much lower than the range of $I_{yy}$ values for the COROTUB. The material properties used to evaluate the performance of the CTM tower designs are shown in Table 3. Note that the design parameters shown in Table 2, including the max eccentricity and deflection limit, remain unchanged in the parametric performance comparison between designs A and B.

**Table 3 Material Properties for CTM Tower.**

| Property | Symbol | Value(s) | Units |
|---|---|---|---|
| Boom Linear Mass Density | $\rho$ | 0.061 | kg/m |
| Boom Elastic Modulus | $E$ | 55.46 | GPa |
| Boom Second Moment of Area | $I$ | $2.335 \times 10^{-8}$ | $m^4$ |

Before performance comparisons can be made, the allowable tip mass must be modified to account for the constant flexural stiffness, $EI$, of the CTM booms. Instead of using the Rayleigh-Ritz method to approximate the critical buckling load, Eq. 1 can simply be used for $P_{cr}$. Substituting this equation into Eq. 14 yields the allowable tip mass for the reference design B:

$$M_B = \frac{\pi^2 EI}{4gL^2}\left(\frac{e}{w(L)} + 1\right) - \frac{3}{10}\rho L \tag{29}$$

For the cable-stayed design A, the corrective tip deflection, $w_c(L)$, in Eq. 27 can be replaced with the uniform cantilevered beam tip deflection equation under a lateral tip load which is:

$$w_c(L) = \frac{T_h L^3}{3EI} \tag{30}$$

Then the updated allowable tip mass for the cable-stayed design A with Eq. 1 substituted in is:

$$M_A = \frac{\pi^2 EI}{4gL^2}\left(\frac{e}{w(L) - \frac{T_h L^3}{3EI}} + 1\right) - \frac{T_x}{g} - \frac{3}{10}\rho L \tag{31}$$

where $T_x$ and $T_h$ are defined as in Eq. 21 and 22, respectively. Note that setting both $T_x$ and $T_h$ to zero recovers the expression for allowable tip mass of an unsupported tower in Eq. 29.

The allowable tip mass, $M_B$, is compared against the maximized $M_A$ with the optimal cable tensions for the CTM lunar towers in Fig. 13 along with the corresponding design A optimal tensions. This figure is generated and formatted identically as Fig. 10, so its description will not be detailed here.

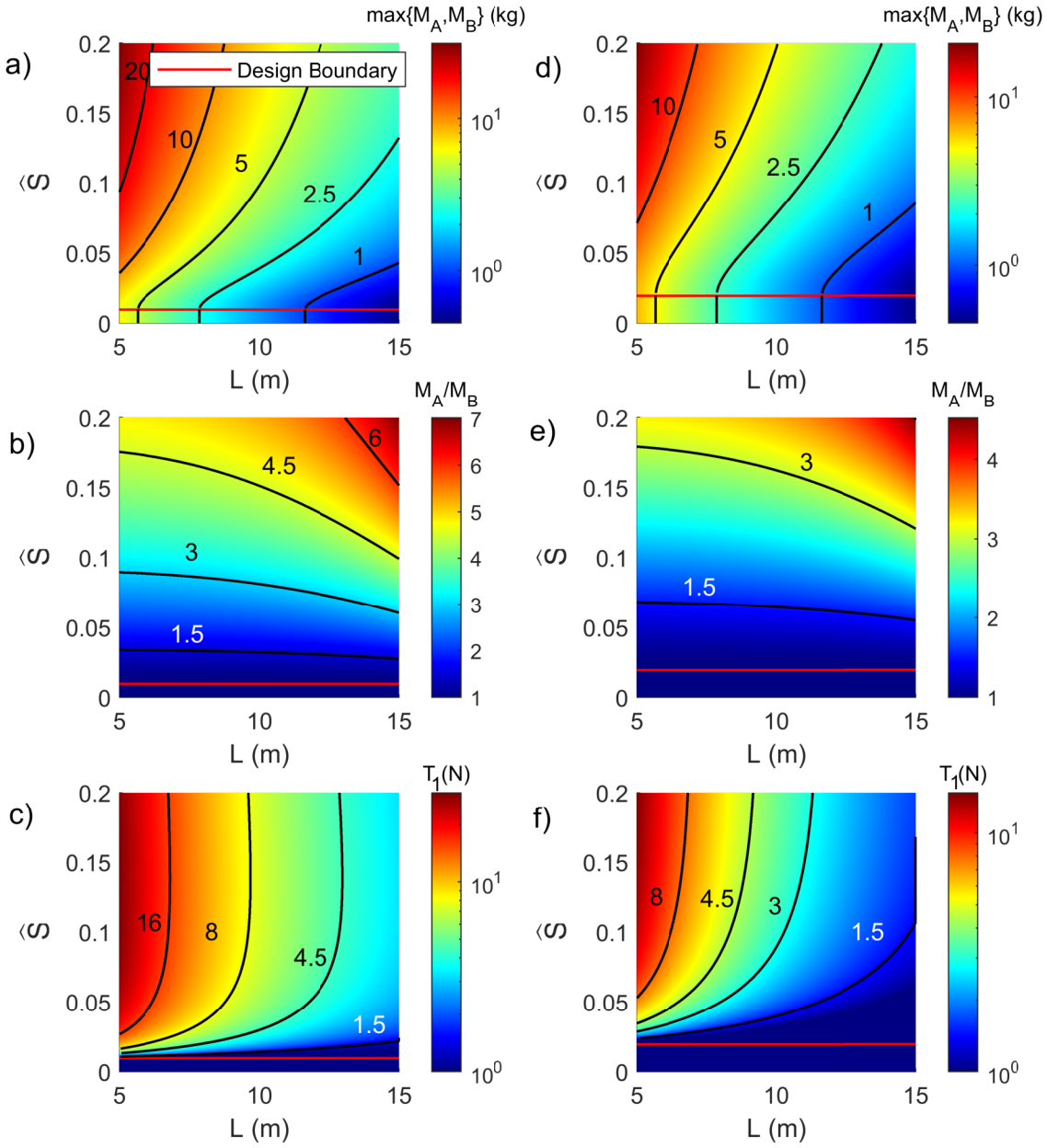


**Fig. 13 Optimized allowable tip mass for CTM lunar towers shown as (a) the maximum of designs A and B, (b) the ratio $\frac{M_A}{M_B}$, and (c) the corresponding optimal tension, $T_1$, of design A as functions of the boom length, $L$, and normalized spreader bar length, $\hat{S}$, for $\theta = 30°$. (d)-(f) are analogous to (a)-(c) except that $\theta = 90°$. $M_A > M_B$ and $M_A = M_B$ above and below the red line, respectively.**

Again, the cable-stayed design A is able to support larger tip masses than the reference design B over the majority of the design space. The specific trends with respect to the boom length $L$, normalized spreader bar length $\hat{S}$, and deflection direction $\theta$ remain unchanged from the COROTUB tower results. The only notable difference is the large reduction in the allowable tip mass for both designs which match the reduction in the optimal cable tensions. This is expected as both the effective elastic modulus $E$ and second moment of area $I_{yy}$ are smaller than those of the COROTUB, with $I_{yy}$ being over an order of magnitude less. This also means that the CTM towers cannot support any tip mass once it reaches a critical boom length as it is lengthened. For this reason, the upper $L$ limit in Fig. 13 is set to 15 m as tower heights beyond this value cannot support any payload of practical interest. The allowable tip mass for the cable-stayed design can be raised if the deflection limit of 3% of the boom length is relaxed.

## V. Conclusions

In this paper, an analytical framework for parametrically quantifying the structural benefit of a cable-stayed lunar tower architecture over an unsupported counterpart is developed. The primary metric is the allowable tip mass that the towers are designed to support as functional payload on the lunar surface. The purpose of the cable-stayed design is to mitigate any tower eccentricity that arise from manufacturing defects, creep, base tilt, and thermal environmental loads. Eccentricity mitigation is achieved by inducing counter deflection with tensioned cables that are connected between the tower tip and three spreader bars at the base deployer. To minimize comparative bias, the load bearing boom is chosen to be a thin-ply composite COROTUB and CTM with identical geometries and material properties between the competing designs. Additionally, the maximum tip deflection limit and estimated initial eccentricity of 3% and 2.75% of the tower height, respectively, are identically imposed between the designs. Since only a small margin is allowed for the delta deflection, the study is considered to be conservative and the allowable tip mass results are on the low range of practical use. Optimal cable tensions are found to exist in the parameter space which maximize the allowable tip mass for the cable-stayed design. Therefore, comparisons are made assuming the cable tensions are always set to their optimized values.

Full comparisons reveal that the cable-stayed lunar tower is able to support larger payloads over the majority of the design space, which consists of the boom length (i.e. tower height) and spreader bar length. The margin of superior load bearing performance increases as the spreader bar is lengthened and the tower height is shortened due to the tensioned cables imposing smaller compressive and larger corrective forces on the boom tip. When the spreader bar length is extremely small relative to the boom length, the optimal tension is zero for the cable-stayed tower, implying that the cables are always detrimental to the allowable tip mass. Without the cables, this tower is functionally no different than the reference unsupported tower. Hence, the load bearing performance is identical for this region of the design space. Practically, the unsupported design is preferable when this is the case as its total system mass and complexity is less than the cable-stayed design.

The effect of the tip deflection direction is also considered. The cable-stayed design is able to support the least amount of weight when its tip deflection is oriented along any of the three spreader bars such that the cables from the remaining two spreader bars equally load the boom. Conversely, if the tip deflection is directed right between two spreader bars such that only a single cable from the remaining spreader bar acts on the boom, then the cable-stayed design is able to support the most amount of weight. This difference is reflected in the allowable tip mass comparisons between the competing architectures.

## Acknowledgments

This research is supported by the Department of Mechanical and Aerospace Engineering and the College of Engineering at North Carolina State University as well as the Space Act Agreement SAA1-35642_Annex_1 with NASA Langley Research Center.

## References

[1] Miller, A. S., Lordos, G., Portman, V. P., Studstill, A., Rohrbaugh, J., Schoeman, W., Williams, C., Rutherford, E., Stamler, N., Zhang, J. Z., Patel, P. B., Martell, B. C., de Weck, O., Hoffmann, J., and Fernandez, J. M., "Design and Development of a Stable, Lightweight, Tall, and Self-Deploying Lunar Tower," 2023 IEEE Aerospace Conference, 2023.

[2] Fernandez, J. M., and Volle, C. E., "Corrugated Rollable Tubular Booms," AIAA Scitech 2021 Forum, 2021.

[3] Lee, A. J., and Fernandez, J. M., "Inducing Bistability in Collapsible Tubular Mast Booms with Thin-ply Composite Shells," *Composite Structures*, Vol. 225, 2019.

[4] Lee, A. J., Fernandez, J. M., and Daye, J. G., "Bistable Deployable Composite Booms With Parabolic Cross-Sections," AIAA Scitech 2022 Forum, 2022.

[5] Stohlman, O. R., Zander, M. E., and Fernandez, J. M., "Characterization and Modeling of Large Collapsible Tubular Mast Booms," AIAA Scitech 2021 Forum, 2021.

[6] Fernandez, J. M., "Advanced Deployable Shell-Based Composite Booms for Small Satellite Structural Applications Including Solar Sails," 4th International Symposium on Solar Sailing, 2017.

[7] Fernandez, J., Krizan, S., and Dyke, R., "Thin-Shell Deployable Composite Booms for Solar Sails: Design, Manufacturing and Qualification," 5th International Symposium on Solar Sailing, 2019.

[8] Wilkie, W. K., Fernandez, J. M., Stohlman, O. R., Schneider, N. R., Dean, G. D., Kang, J. H., Warren, J. E., Cook, S. M., and Heiligers, M. J., "Overview of the NASA Advanced Composite Solar Sail System (ACS3) Technology Demonstration Project," AIAA Scitech 2021 Forum, 2021.

[9] Brinkmeyer, A., Pellegrino, S., and Weaver, P. M., "Effects of Long-term Stowage on the Deployment of Bistable Tape Springs," *Journal of Applied Mechanics*, Vol. 83, No. 1, 2016.

[10] Salazar, J. E., and Fernandez, J. M., "Experimental Characterization of the Dimensional Stability of Deployable Composite Booms During Stowage," AIAA Scitech 2021 Forum, 2021.

[11] Hedgepeth, J. M., "Critical Requirements for the Design of Large Space Structures," 2nd Conference on Large Space Platforms: Toward Permanent Manned Occupancy in Space, 1981.

[12] Belvin, W. K., "Analytical and Experimental Vibration and Buckling Characteristics of a Pretensioned Stayed Column," *Journal of Spacecraft and Rockets*, Vol. 21, 1984, pp. 456–462.

[13] Campbell, T. G., Bailey, M. C., and Belvin, W. K., "The Development of the 15-Meter Hoop Column Deployable Antenna System With Final Structural and Electromagnetic Performance Results," *Acta Astronautica*, Vol. 17, 1988, pp. 69–77.

[14] Jones, T. C., Watson, J. J., Mikulas, M., and Bart-Smith, H., "Design and Analysis of Tension-Aligned Large Aperture Sensorcraft," 49th AIAA/ASME/ASCE/AHS/ASC Structures, Structural Dynamics, and Materials Conference, 2008.

[15] Greschik, G., and Mikulas, M., "Design Study of a Square Solar Sail Architecture," *Journal of Spacecraft and Rockets*, Vol. 39, No. 5, 2002, pp. 653–661.

[16] Banik, J. A., and Maji, A. K., "Structural Scaling Parameters for Rectangular Flexible Blanket Solar Arrays," *Journal of Spacecraft and Rockets*, Vol. 53, No. 5, 2016, pp. 936–951.

[17] Lee, A., and Pellegrino, S., "Cable-Stayed Architectures for Large Deployable Spacecraft," AIAA Scitech 2021 Forum, 2021.

[18] Lee, A. J., and Pellegrino, S., "Mass Efficiency of Strip-Based Coilable Space Structures," *International Journal of Solids and Structures*, Vol. 254-255, 2022.

[19] Timoshenko, S. P., and Gere, J. M., *Theory of Elastic Stability*, Dover Publications, 1961.